ACS APPLIED MATERIALS & INTERFACES

Research Article

www.acsami.org

Interfacial Cyclic Fatigue of Atomic-Layer-Deposited Alumina Coatings on Silicon Thin Films

Eva K. Baumert and Olivier N. Pierron*

George W. Woodruff School of Mechanical Engineering, Georgia Institute of Technology, Atlanta, Georgia 30332-0405, United States

ABSTRACT: A microresonator-based interfacial fatigue testing technique was used to investigate the subcritical delamination of atomic-layer-deposited alumina coatings along the sidewalls of deep-reactive-ion-etched monocrystalline silicon thin films. This technique ensures loading conditions relevant to microelectromechanical system devices, including kHz testing frequency and fully reversed cyclic stresses. Four different coating thicknesses (4.2, 12.6, 25, and 50 nm) were investigated in two environments (30 °C, 50% relative humidity (RH) and 80 °C, 90% RH). Fatigue damage, in the form of channel cracks and delamination of the alumina coating, was found to accumulate slowly over more than 1×10^8 cycles. The average delamination rates increase with increasing energy release rate amplitude for delamination, modeled with a power law relationship. In the harsher environment, the rates are roughly 1 order of magnitude higher. Additionally, a few tests under static load were conducted for which no delamination (or crack growth) occurred, demonstrating that the governing interfacial fatigue mechanism is cycle-dependent.

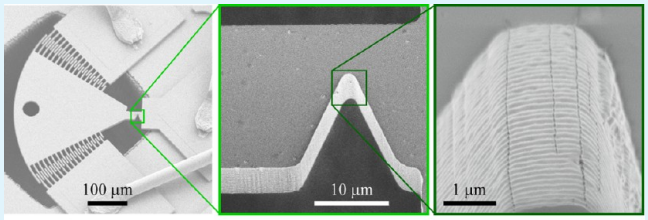

ALD alumina-coated silicon microresonator with fatigue damage of the coating localized at the notch root.

KEYWORDS: *interfacial fatigue, delamination, ALD, alumina, microresonator, harsh environments*

1. INTRODUCTION

The reliability of silicon-based microelectromechanical systems (MEMS) continues to be a determining factor for their successful commercialization. Often, MEMS devices require expensive hermetic packaging to prevent early degradation of the thin film materials, including silicon. These packaging solutions cannot always be employed, for example, for (bio)chemical MEMS sensors that require direct exposure to the surrounding environment.[1] An alternative consists of encapsulating MEMS components with ultrathin protective coatings, such as those processed via atomic layer deposition (ALD).[2−4] For example, ALD alumina (Al_2O_3) has been shown to significantly improve both wear-resistance[5] and fatigue resistance[6,7] of silicon MEMS. In these instances, the reliability of the MEMS devices hinges upon the structural reliability of the ALD coating, such as cracking and delamination from the underlying thin films (interfacial fracture or fatigue). A representative testing technique must be employed to properly study the interfacial fracture and fatigue behavior of ALD-coated MEMS devices, including high testing frequencies, accumulation of billions of cycles, testing in both "mild" and "harsh" environments, negative load ratio (R = minimum stress/maximum stress), and surface roughness.

Interfacial fracture in thin films has been the subject of numerous studies,[8−15] some of which reported time-dependent delamination growth.[9,16,17] Fewer studies also investigated interfacial fatigue (possibly because of the experimental difficulties mentioned above), most prominently of metal/ceramic systems.[8,13,16,18,19] Classical metal fatigue was found to drive the observed interfacial fatigue[8,16] and interfacial fatigue crack growth was found to occur at lower strain energy release rates than interfacial fracture under static loading.[16] Some studies also reported that the interfacial strength is reduced in harsher environments, both under static loading or displacement[9,10,17] and cyclic loading.[18,19] With respect to ALD coatings, many investigations have so far focused on the monotonic[20−24] and thermomechanical properties[25] of ALD coatings, but little is known about their cyclic degradation properties[26,27] even though MEMS are inherently subjected to cyclic loading. Particularly, the interfacial fatigue properties (or subcritical delamination) of ultrathin ALD coatings on silicon thin films have been largely unexplored so far. The present study discusses the subcritical delamination of model ALD Al_2O_3 coatings (ranging from 4.2 to 50 nm in thickness) from silicon thin films under the influence of static and cyclic loading in both a mild and a harsh environment; the cohesive fatigue properties of the same coatings have already been published.[27] The use of a silicon MEMS resonator to investigate these properties ensures relevant loading conditions, including kHz testing frequency and fully reversed cyclic stresses.

Section 2 details both the experimental techniques for the cyclic and static tests as well as the finite element modeling (FEM) necessary to calculate delamination growth rates. Section 3 presents the experimental fatigue results in the form of resonance frequency (f_0) evolution plots and scanning electron microscopy (SEM) images, the results from testing

Received: April 2, 2013
Accepted: May 30, 2013
Published: May 30, 2013

   dx.doi.org/10.1021/am4011989 | ACS Appl. Mater. Interfaces 2013, 5, 6216−6224

under static load, the FEM results, and the calculated delamination rates. The last two sections discuss the results and possible governing mechanisms and conclude the paper with a short summary of the findings.

2. EXPERIMENTAL METHODS

The limited number of studies on interfacial fatigue crack growth in thin film materials is in part related to the experimental challenges associated with the measurement of these properties. Time- and cycle-dependent interfacial crack growth rates of thin film stacks that are relevant to the microelectronics industry have already been measured using double-cantilever beam specimens[16] or sandwich four-point flexure specimens.[9,28] These techniques are not suitable to study delamination in silicon-based MEMS structures, which can be subjected to high frequency (kHz and above) fully reversed cyclic stresses. A recently developed promising technique for interfacial fatigue studies at high frequencies is the magnetically actuated peel test for thin films.[15] However, that technique may not be suitable to study the fatigue delamination occurring along the rough sidewalls of deep reactive ion etched (DRIE) silicon films, which is the configuration of interest in the present study. Hence, a simple ALD alumina-coated MEMS structure was employed to study the fatigue-induced delamination between the ALD coating and the sidewalls of DRIE silicon films. Large, high frequency (40 kHz) fully reversed cyclic stresses were applied to a localized region along the sidewall of the DRIE silicon film; the extent of coating cracking and delamination was monitored via precise f_0 measurements. Delamination rates could then be calculated by combining the experimental results with FEM results. This technique had already been used to calculate the cohesive fatigue crack propagation rates of the coatings.[27]

The experimental details are provided below.

2.1. Microresonators. Testing was conducted on freestanding 10 μm thick monocrystalline silicon microresonators fabricated from a (100) silicon-on-insulator wafer. The microresonators, depicted in Figure 1, consist of a [100]-oriented notched cantilever beam (notch root radius $\approx$ 1 μm) attached to a fan-shaped mass and two comb drives (interdigitated fingers on each side of the mass); one of the comb drives allowed for electrostatic actuation and the other for capacitive motion sensing.[29] Figure 1c depicts the scalloped sidewall of the silicon resonators that is typical for the DRIE process. These features were reported to be 38.4 nm deep and approximately (230 $\pm$ 40) nm spaced apart.[30]

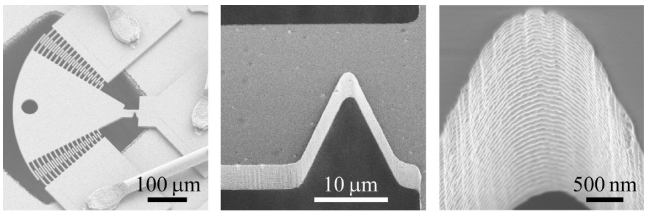

(a) Microresonator (b) Notched beam (c) Notch root sidewall

Figure 1. SEM images of a 20°-tilted microresonator revealing the scalloped sidewall, resulting from the silicon etching process.

2.2. Atomic Layer Deposition. The microresonators were coated with four different alumina coating thicknesses in an in-house ALD tool, using trimethyl aluminum (TMA) and water as precursors. The pulse durations for water and TMA were 10 and 17 ms at a deposition temperature of 200 °C. The numbers of cycles for the four alumina thicknesses were 30, 90, 179, and 358, corresponding to nominal thicknesses ($h_{Al_2O_3}$) of 4.2, 12.6, 25, and 50 nm, respectively. Although not specifically measured in this study, the equal-biaxial residual stress and strain in the coatings can be expected to be in the range of 300–350 MPa, corresponding to 0.22–0.26% strain for a deposition temperature of 200 °C.[3]

2.3. Fatigue Test Protocol. The fatigue tests were performed at resonance (in-plane resonance frequency f_0 ~40 kHz), leading to fully reversed sinusoidal in-plane bending of the notched beam. Under these conditions, fatigue damage develops at the notch root because of geometric stress concentrations.[29] A sinusoidal signal (without offset) was applied to one comb structure to actuate the electrically grounded beam-mass assembly via electrostatic forces. The second comb structure was used to track the second-harmonic induced currents, thus providing a metric for the amplitude of rotation. The sinusoidal input voltage was applied with a waveform generator (Agilent 33220A 20 MHz) and amplified with a high-voltage amplifier (AVTECH-110G). A 50 V dc bias voltage was applied to the sensing comb structure, resulting in induced currents (~nA level) during cyclic motion, which were amplified and converted to a voltage with a custom-made, off-chip, current-to-voltage amplifier circuit containing an operational amplifier (OPA 128). This output voltage was then measured with a lock-in amplifier (SR830–100 kHz DSP synchronized with the waveform generator) at the second harmonic of the input sinusoidal voltage. The measurements were performed in a controlled environment using a temperature and humidity chamber (ESPEC SH-241 Bench-top Type), with a 0.1 °C, 1% RH resolution at either 30 °C, 50% relative humidity (RH) or 80 °C, 90% RH.

The resonator's f_0 was periodically measured during a fatigue test, by sweeping over a range of frequencies around the expected value and monitoring the output signal, which is proportional to the amplitude of rotation of the structure, as a function of excitation frequency. A second order polynomial fit was used to find the peak output, and the corresponding frequency was defined as f_0. The precision in f_0 measurement was typically ~0.2 Hz. The excitation frequency was adjusted to match f_0 after every f_0-measurement during the fatigue test. The tests are considered amplitude-controlled (and thus both stress- and strain-controlled given the devices' elastic behavior) because the output voltage was typically stable during the tests.

A combination of finite element analysis and optical calibration was used to calculate the applied strain at the notch root (ε_a) along the direction of the silicon film's plane (in-plane bending of the notched beam). The optical calibration was performed in laboratory air prior to each specimen's fatigue test using a digital camera (JAI-PULNiX RM-1402CL) and objective (50× Mitutoyo Plan Apo SL Series) to record the motion blur of the oscillating resonator at the outermost combs, from which the angle of rotation was then calculated.[31] Linear-elastic FEM was used to correlate the angle of rotation to the maximum principal coating strain at the notch root, which resulted in the following relationship: $\varepsilon_a = c/\theta$ where ε_a is in percent, θ is in radians, and c is 70.73 rad^{-1} for $h_{Al_2O_3}$ = 4.2 nm, 70.99 rad^{-1} for $h_{Al_2O_3}$ = 12.6 nm, 71.37 rad^{-1} for $h_{Al_2O_3}$ = 25 nm, and 72.22 rad^{-1} for $h_{Al_2O_3}$ = 50 nm. The optical calibration was performed at multiple, but low (nondamaging) strain amplitudes. The angle of rotation applied during the test can be extrapolated given the observed linear relationship between the output voltage (which is proportional to the maximum strain amplitude) and the input voltage.[32] The optical calibration's precision is 0.3 mrad or 0.02% strain.

2.4. Strain Energy Release Rate Calculation for Delamination and Mode Mixity. The strain energy release rate amplitude (G_a) associated with the delamination of the ALD coating from the silicon film's sidewall is approximated with the classical formula for delamination of a thin film from its substrate under residual strain according to[33]

$$G_a = \frac{1}{2}\bar{E}_{Al_2O_3}\varepsilon_a^2 h_{Al_2O_3} \quad (1)$$

where $\bar{E}_{Al_2O_3}$ is the plain strain modulus ($(E)/(1-\nu^2)$) of Al_2O_3 and ε_a is the strain amplitude at the notch root. Here, the applied strains are employed instead of the residual strain given that they are at least 5 times larger. The use of this formula is in part justified by the fact that, along the silicon sidewall, the nanoscale coatings are much thinner than the lateral dimensions along which the large strains are applied. While not completely accurate, (the effects of the scallops are ignored) this formula should capture the main effects of coating thickness and applied strains on the driving force for delamination.

Under these simplifying conditions, the mode mixity (a measure for the relative amounts of shear (mode II) to opening load (mode I)) has been calculated as a function of the Dundur's parameters, α and β:

$$\alpha = \frac{\bar{E}_{Al_2O_3} - \bar{E}_{Si}}{\bar{E}_{Al_2O_3} + \bar{E}_{Si}} \quad (2)$$

$$\beta = \frac{1}{4}\left[\frac{\bar{E}_{Al_2O_3}(1-\nu_{Al_2O_3})(1-2\nu_{Si}) - \bar{E}_{Si}(1-\nu_{Si})(1-2\nu_{Al_2O_3})}{\bar{E}_{Al_2O_3}(1-\nu_{Al_2O_3})(1-2\nu_{Si}) + \bar{E}_{Si}(1-\nu_{Si})(1-2\nu_{Al_2O_3})}\right] \quad (3)$$

where $\bar{E}_{Si}$ is the plain strain modulus of silicon and $\nu_{Al_2O_3}$ and ν_{Si} are the Poisson's ratios of alumina and silicon, respectively. Given the similar elastic properties of Al_2O_3 and silicon (155 GPa $\leq E_{Al_2O_3} \leq$ 195 GPa[3,20] and $E_{Si} \approx$ 130 GPa (in the (100) plane and [100] direction) as well as $\nu_{Al_2O_3}$ = 0.23 and 0.218 $\leq \nu_{Si} \leq$ 0.228[34]), both α and β can be approximated as 0, which corresponds to an approximate phase angle ψ of 52.1°.[35]

2.5. Static Loading Test Protocol. The high quality factor of the microresonators ($Q \approx$ 750 at 30°, 50% RH[36]) inhibits static electrostatic testing of the resonators because too high input voltages would be required. Instead, a couple of resonators were displaced manually to investigate the static fatigue behavior under constant load. For this purpose, a probe tip (Micromanipulator model 7A-M) was mounted to a leadscrew stage (Edmund Optics, Small X-Y-Z Axis Leadscrew Drive Stage) on a vibration-isolated table (Thorlabs ScienceDesk), which allowed insertion of the tip through the large hole in the resonator mass (see Figure 1a) and precise in-plane tensile or compressive displacement of the latter. The displacement was monitored and recorded using the optical microscope setup mentioned above. The angle of rotation of every specimen was calculated from a comparison of pictures at rest and at full displacement, which then allowed calculation of the static strain at the notch root (ε_s) with a precision of approximately 0.3 mrad or 0.02% strain. The tests under static load were conducted in laboratory air. The resonance frequency of the tested specimens was determined right before and right after the static tests in order to assess the amount of damage accumulated under static loading.

2.6. Finite Element Modeling. Linear elastic FEM was used to investigate the influence of crack channeling and delamination of the coating on f_0. This information is necessary to calculate the extent of fatigue damage (crack length, delaminated length) and the corresponding fatigue crack growth rates based on the experimental results (f_0 evolution and post-test SEM observations). The FE model consisted of a 2D geometry of the silicon resonator mass and notched beam;[27] only the beam was uniformly coated with alumina. The assumption of a 2D analysis is that the fatigue delamination occurs homogeneously along the channeled cracks, which is consistent with the majority of inspected cracks. The model was constrained at the base of the beam by setting all displacements to zero. For the static analysis, a pressure was applied to the comb instead of an electrostatic force. The analysis with ANSYS 14.0 used PLANE183 elements to mesh the area, which was most finely meshed around the crack or delamination, respectively, until convergence of the results was achieved. For the analysis, published data was used for the elastic properties of monocrystalline silicon (linear orthotropic properties in the (100) plane and [100] direction: C_{11} = 165.64 GPa, C_{12} = 63.94 GPa, and C_{44} = 79.51 GPa[34]) and alumina (reported values for the Young's modulus of alumina range from 155 GPa to 195 GPa). The uncertainty in elastic modulus of the alumina was accounted for in the FE analysis.

A block Lanczos method was used to extract f_0 from models with the four different coating thicknesses in order to compare these values with the measured f_0 data. f_0 was also modeled for the case of a crack extending through 99% of the coating thickness as well as delamination. Figure 2b illustrates that delamination is modeled by removing an area of coating. The influence of delamination on f_0 was investigated for delamination extents (arc lengths λ) of one, two, five, and ten times $h_{Al_2O_3}$ to both sides of a crack. The influence of crack angle (β) and distance from the notch root (d) as shown in Figure 2a were investigated as well as the influence of the delamination's location, shown in Figure 2b.

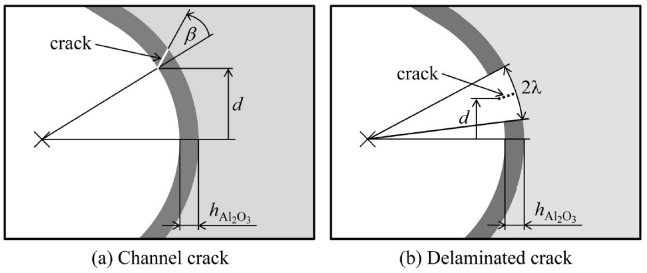

(a) Channel crack (b) Delaminated crack

Figure 2. Schematic of the alumina-coated notch root. The light gray represents the silicon resonator; the dark gray represents the coating. Dimensions not to scale. (a) Illustration of crack angle β and distance d. β is measured relative to a crack that penetrates the coating perpendicularly, whereas d is the distance of the crack from the notch root. (b) Illustration of delamination extent λ (of a delaminated, channeled crack) and distance d to the notch root.

3. RESULTS

This section presents the results of the cyclic and static fatigue experiments on the alumina-coated silicon resonators, coating damage observations, and FEM results that were combined with the f_0 evolution plots to calculate the coatings' fatigue delamination rates.

3.1. Resonance Frequency Evolution During Cyclic and Static Tests. *3.1.1. Behavior Under Cyclic Loading.* ALD alumina coatings were previously shown to have a significant effect on the general fatigue behavior of the silicon microresonators.[6,7] Summarizing the findings, the presence of the ALD coatings leads (a) to a significant increase in fatigue life of silicon, and (b) to a characteristically different f_0 evolution curve with (c) larger total changes in f_0. On the basis of these results, the testing of ALD-coated silicon microresonators can be used to calculate the fatigue degradation properties of ALD coatings, as explained next.

Figure 3 shows a representative f_0 evolution curve for each test condition; a thin red line represents testing performed at

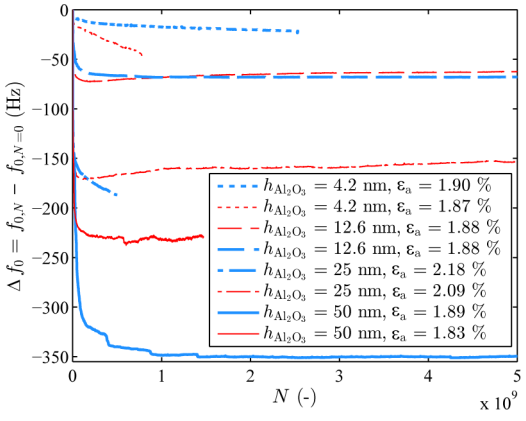

Figure 3. Examples of f_0 evolution plots for the four different coating thicknesses and two environments (wider blue lines denote 30 °C, 50% RH, thin red lines denote 80 °C, 90% RH).

dx.doi.org/10.1021/am4011989 | ACS Appl. Mater. Interfaces 2013, 5, 6216−6224

80 °C, 90% RH and a thicker blue line represents testing performed at 30 °C, 50% RH for each of the four different coating thicknesses. For all microresonators, the frequency decreases rapidly during the first 10^8 cycles. It then decreases at a much lower rate for $h_{Al_2O_3}$ = 4.2 nm and stabilizes for $h_{Al_2O_3}$ = 12.6 nm thick or thicker, having a small but nonzero positive or negative slope.[7] Some resonators fractured before reaching this frequency evolution plateau, such as the 25 nm thick resonator tested in the mild environment in Figure 3. The maximum change in f_0 ($\Delta f_{0,max}$) is plotted in Figure 4 and increases with

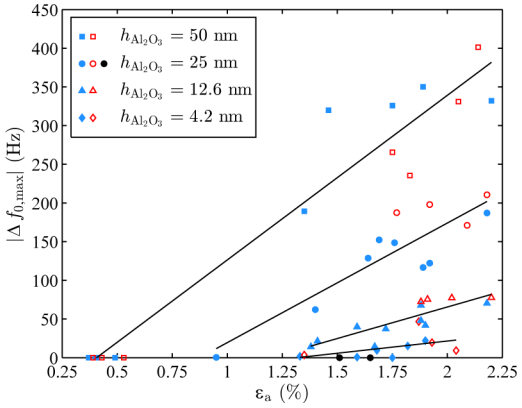

Figure 4. Maximum decrease in f_0 as a function of applied strain (solid (light blue) symbols denote 30 °C, 50% RH, outlined (red) symbols denote 80 °C, 90% RH). The solid black symbols denote the tests performed under static load on the 25 nm Al_2O_3-coating.

increasing $h_{Al_2O_3}$ and ε_a, but seems to be independent of the environment (in contrast to the uncoated devices).[6,7] Linear fits were added to Figure 4 to highlight the overall trends. On the basis of these observations, the steep initial decrease in f_0 is attributed to damage of the Al_2O_3, allowing the probing of its cyclic fatigue properties.

3.1.2. Behavior under Static Loading. Static loading of resonators coated with $h_{Al_2O_3}$ = 25 nm at ε_s = 1.51% (corresponding to a static strain energy release rate (G_s) of 0.53 N m^{-1}) was performed on a virgin resonator for 3 h and did not result in any changes in f_0. This result indicates that neither crack initiation nor crack growth nor delamination occurs under static loading, while it does under cyclic loading. Fatigue testing at $\varepsilon_a = \varepsilon_s$ = 1.51% would lead to significant Δf_0 values of −100 Hz.[27] Static testing was also performed on a briefly fatigued 25 nm alumina-coated resonator with the intention of creating an initial crack in the coating to subsequently study delamination under monotonic load. The fatigue test was conducted for only 1.85 × 10^7 cycles at ε_a = 1.50% (or G_a of 0.52 N m^{1-}) which led to a decrease in f_0 by 52.4 Hz. The subsequent application of first tensile and then compressive strains of ε_s = 1.65% (corresponding to a G_s of 0.63 N m^{-1}) and −1.60% for 3 h each did not alter the device's f_0. These results shows that delamination does not occur under static loads of either tensile or compressive strains alone, whereas it does occur under cyclic strains of the same magnitude.

The time span of 3 h of static testing was chosen for the following reason: 3 h of pure cyclic testing (i.e., without frequency sweeps) corresponds to 4.3 × 10^8 cycles, at which point Δf_0 has about reached its maximum for the majority of tested resonators. Under cyclic loading, however, the notch root's exposure to the maximum strain amplitude is much less than 3 h;[37] so if static loading damage were the reason for the observed changes in f_0 during the performed cyclic testing, similar Δf_0 values should be observed after static testing at the same applied strain for 3 h.

3.2. Coating Damage Observations. Figure 5 shows SEM images of fatigued resonators, featuring severe coating

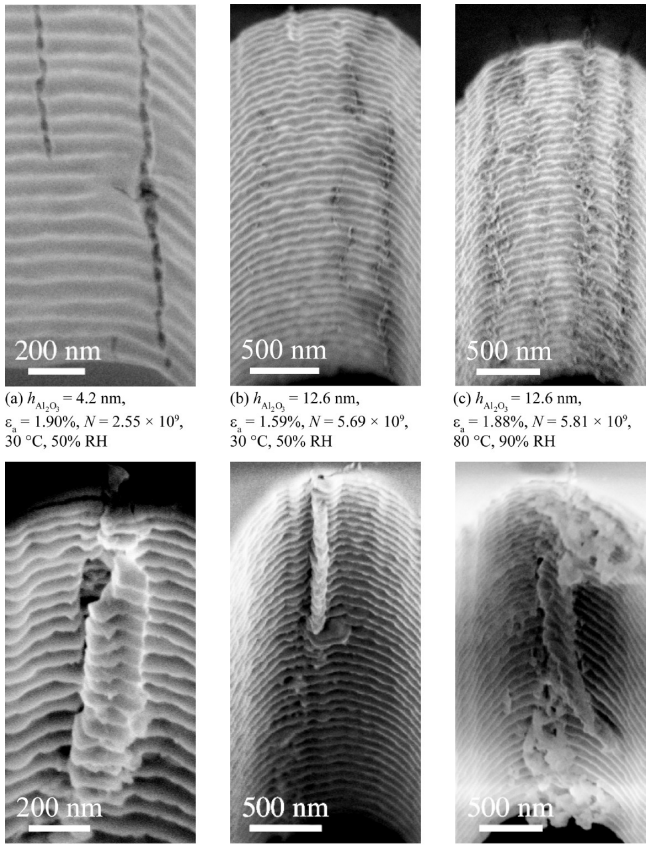

(a) $h_{Al_2O_3}$ = 4.2 nm, ε_a = 1.90%, N = 2.55 × 10^9, 30 °C, 50% RH
(b) $h_{Al_2O_3}$ = 12.6 nm, ε_a = 1.59%, N = 5.69 × 10^9, 30 °C, 50% RH
(c) $h_{Al_2O_3}$ = 12.6 nm, ε_a = 1.88%, N = 5.81 × 10^9, 80 °C, 90% RH
(d) $h_{Al_2O_3}$ = 50 nm, ε_a = 2.20%, N = 8.01 × 10^9, 30 °C, 50% RH
(e) $h_{Al_2O_3}$ = 50 nm, ε_a = 1.75%, N = 5.26 × 10^9, 30 °C, 50% RH
(f) $h_{Al_2O_3}$ = 50 nm, ε_a = 1.75%, N = 1.23 × 10^9, 80 °C, 90% RH

Figure 5. SEM images showing delamination at the beam's notch root and differences in appearance due to the environment.

damage in the form of delaminated cracks. Figure 5a shows a detail of a specimen coated with 4.2 nm Al_2O_3; the crack faces are visibly spaced apart, which is likely due to the release of tensile residual stresses in the coating in combination with some delamination surrounding the crack. Comparing Figures 5b, 5c, 5e, and 5f, it is evident that the testing environment affects the damage appearance: for the same coating thickness and similar strain amplitude, more alumina pieces seem to break off when fatigued in the harsh environment. Images b and c in Figure 5 also show that the number of cracks scales with ε_a (see also ref 27). The 50 nm thick coating shows the largest extent of delamination and entire coating pieces have broken off, see Figure 5d–f. Further evidence of delamination can also be seen in the form of cracks at the corner between sidewall and top surface of the microresonators, e.g., in Figure 5d). Summarizing, the following trends were observed: (a) the extent of delamination scales with $h_{Al_2O_3}$, (b) more damage is observed after testing in the harsh environment, and (c) testing at higher ε_a leads to more cracks.

dx.doi.org/10.1021/am4011989 | ACS Appl. Mater. Interfaces 2013, 5, 6216–6224

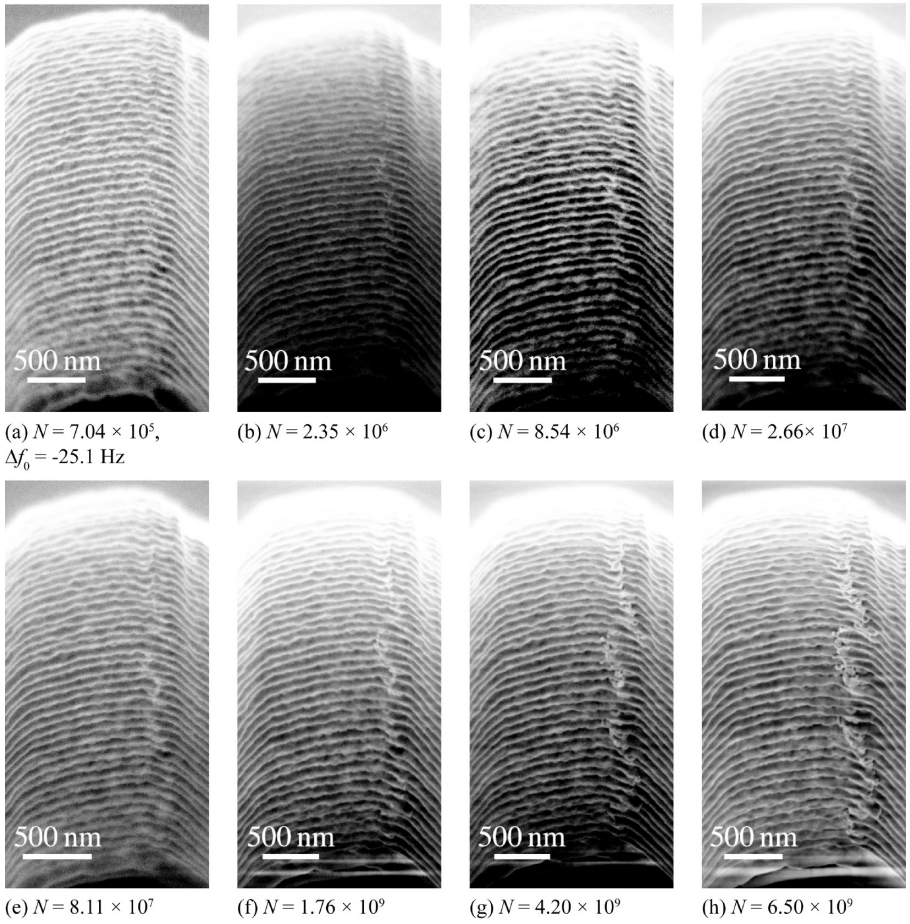

(a) $N = 7.04 \times 10^5$, $\Delta f_0 = -25.1$ Hz (b) $N = 2.35 \times 10^6$ (c) $N = 8.54 \times 10^6$ (d) $N = 2.66 \times 10^7$

(e) $N = 8.11 \times 10^7$ (f) $N = 1.76 \times 10^9$ (g) $N = 4.20 \times 10^9$ (h) $N = 6.50 \times 10^9$

Figure 6. SEM images taken during interruptions of a test conducted at ε_a = 1.56%, 30 °C, 50% RH on a specimen coated with 25 nm alumina.

To investigate the coating damage evolution during cycling, a test at ε_a = 1.56% on a specimen coated with 25 nm alumina was interrupted seven times for SEM imaging. The SEM images taken after each test segment are depicted in Figure 6. The first SEM image (Figure 6a) was taken after only 7.04×10^5 cycles and a corresponding Δf_0 of −25.1 Hz. Although initial damage is visible, a clear crack could not be seen; the reason for this is likely that the resonator is at rest during SEM imaging and a fine crack would therefore be closed. The second image (Figure 6b) was taken after 2.35×10^6 cycles and it appears that small elevated features increased in size along the line that appears damaged. These elevated features grow with continued cycling, as can be seen in the sequence of SEM images. The evolution of f_0 after the first interruption and SEM imaging could not be measured accurately due to what is believed to be electron beam-induced charging of the ALD coating. It is, however, believed that this particular fatigue test was representative of the other fatigue tests with no interruption for SEM imaging. Hence, this result shows that the damage accumulates slowly rather than instantaneously. A likely scenario of events is that a crack channels before the coating starts to delaminate from the silicon thin film.

3.3. Finite Element Analysis. FEM was performed to further quantify the effect of coating cracking and delamination on f_0. Experimental observations show that an increase in $h_{Al_2O_3}$ leads to an increase in the resonators' initial f_0, which is also confirmed by FEM and shown in Figure 7. This figure compares the measured and simulated results in a f_0 vs $h_{Al_2O_3}$ plot. The thicker the coating, the higher f_0; the average f_0 for $h_{Al_2O_3}$ = 50 nm is 1332 Hz higher than for $h_{Al_2O_3}$ = 4.2 nm thick coating. The error bars of the experimental data represent their standard deviation, which is relatively large because small geometric differences have a large effect on f_0.[30] FEM predicts an average increase in f_0 of 830 Hz from 4.2 to 50 nm, and the error bars correspond to the range of values assumed for the elastic modulus of the ALD alumina (155 GPa ≤ $E_{Al_2O_3}$ ≤ 195 GPa). The prediction lies within the standard deviation of the experimental values for all four coating thicknesses, thereby

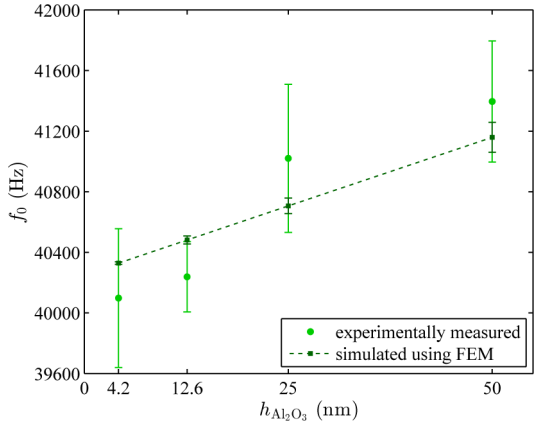

Figure 7. Influence of coating thickness on the initial resonance frequency.

validating the FEM. However, the actual value of $E_{Al_2O_3}$ cannot be inferred from comparing the FEM results with the experiments given the large experimental scatter. Hence, $E_{Al_2O_3}$ was arbitrarily chosen to be 175 GPa based on the literature values. Additional measurements would be required to measure $E_{Al_2O_3}$ independently.[20]

Given the reasonable match of experimental and modeled effect of the coating thickness on f_0, FEM was also used to calculate the effects of coating cracking and delamination on f_0. The analysis confirms that a crack in the coating leads to a reduction in stiffness and f_0 compared to undamaged coated resonators. FEM showed that a crack extending through 99% of the coating thickness at the notch root corresponds to the following changes in f_0 (i.e., $f_{0,\text{ uncracked}} - f_{0,\text{ 99\%cracked}}$): (49.2 ± 7.0) Hz for $h_{Al_2O_3}$ = 50 nm, (13.0 ± 1.9) Hz for $h_{Al_2O_3}$ = 25 nm Al_2O_3, (3.4 ± 0.6) Hz for $h_{Al_2O_3}$ = 12.6 nm Al_2O_3, and (0.5 ± 0.1) Hz for $h_{Al_2O_3}$ = 4.2 nm Al_2O_3. The uncertainty arises from $E_{Al_2O_3}$.

Figure 8 shows that the angle at which a crack penetrates the coating (see Figure 2a) is of negligible influence even for the thickest coating, stiffest modulus, and angles β deviating up to 60° from perpendicular. Under these conditions, a maximum difference in Δf_0 of ±0.5 Hz was found compared to the total change of 56.2 Hz for a centered crack.

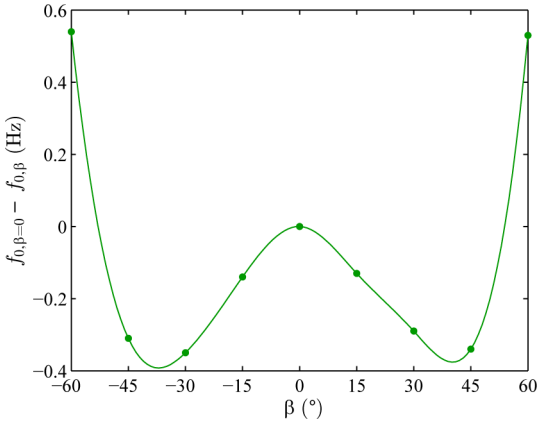

Figure 8. FEM analysis of the influence of crack angle β on f_0 for $h_{Al_2O_3}$ = 50 nm and E = 195 GPa.

FEM was also used to simulate a delaminated crack in the different coatings. The results are displayed in Figure 9: the absolute change in f_0 for one single delaminated crack ($\Delta f_{0,\text{ 1crack}} = f_{0,\text{ no crack}} - f_{0,\text{ delaminated crack}}$) is plotted against the extent of delamination to both sides of the crack divided by the coating thickness, where λ = 0 corresponds to a crack without delamination. For $h_{Al_2O_3}$ = 50 nm, a delaminated crack changes f_0 by Δf_0 = (284.2 ± 31.9) Hz compared to an uncracked coating when the delaminated area is $10h_{Al_2O_3}$ wide (compared to a change in f_0 of only (49.2 ± 7.0)Hz for a simple nondelaminated crack). For all four thicknesses, Δf_0 increases by a factor of 5−6 for a delaminated crack compared to a simple crack when $\lambda = 10h_{Al_2O_3}$. When multiplying these simulated results with the number of observed cracks on the fatigued resonators, the results are fairly close to the

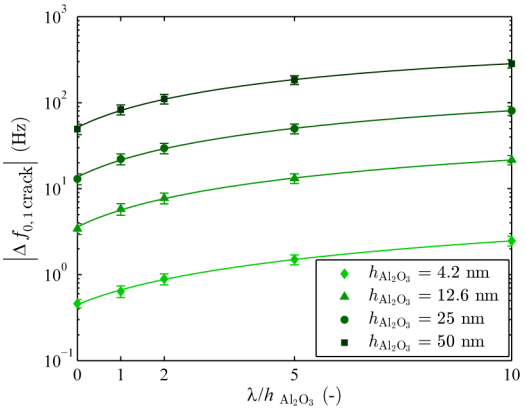

Figure 9. Influence of delamination on f_0, where $\Delta f_{0,\text{ 1crack}} = f_{0,\text{ no crack}} - f_{0,\text{ delaminated crack}}$. The error bars reflect the uncertainty in $E_{Al_2O_3}$.

experimentally measured $|\Delta f_{0,max}|$ values for λ between $5h_{Al_2O_3}$ and $10h_{Al_2O_3}$.[27]

The influence of a delaminated crack that is located at a distance d from the notch root is depicted in Figure 10. The

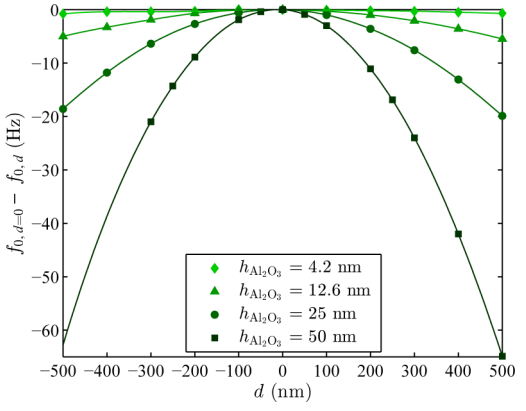

Figure 10. Influence of crack location d on f_0 assuming $\lambda/h_{Al_2O_3}$ = 10 and $E_{Al_2O_3}$ = 175 GPa.

simulations were based on a $E_{Al_2O_3}$= 175 GPa and $\lambda = 10h_{Al_2O_3}$. On the basis of this figure, a delaminated crack 500 nm away from the notch root corresponds to a change in f_0 of 219.3 Hz, whereas a delaminated crack at the notch root corresponds to a change in f_0 of 284.2 Hz (see Figure 9).

3.4. Delamination Rates Calculation. The delamination rates ($d\lambda/dN$) were calculated according to the following procedure:

(1) For every test, the number of fully channeled, fully delaminated cracks was estimated by dividing the experimental $\Delta f_{0,max}$ by the change in f_0 that corresponds to one fully channeled, fully delaminated, centered crack according to FEM, $\Delta f_{0,1crack}$. This was done for both $\lambda/h_{Al_2O_3}$ = 5 and 10 using the data displayed in Figure 9. This simplified approach assumes that n cracks would result in $\Delta f_0 = n\ \Delta f_{0,1crack}$. The effect of crack location along the notch on Δf_0, shown in Figure 10 is neglected to simplify the analysis, and should only have a minor effect given that most cracks are well within the notch root.

(2) The Δf_0 components of the f_0 evolution data, as shown in Figure 11, were divided by the number of cracks to get the equivalent change in f_0 corresponding to one crack.

dx.doi.org/10.1021/am4011989 | ACS Appl. Mater. Interfaces 2013, 5, 6216−6224

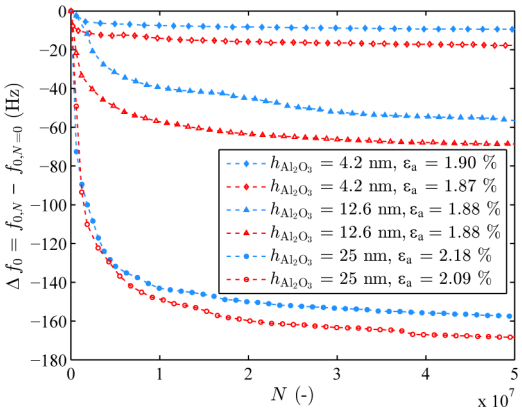

Figure 11. Examples of f_0 evolution plots for three different coating thicknesses and 2 environments. Solid (light blue) symbols denote 30 °C, 50% RH, outlined (red) symbols denote 80 °C, 90% RH.

(3) Figure 9 was fitted with a second degree polynomial for each of the four coating thicknesses. These fit equations were used to calculate the equivalent λ from the above modified frequency evolution data, resulting in delamination evolution data as shown in Figure 12. In this model, the channeled cracks

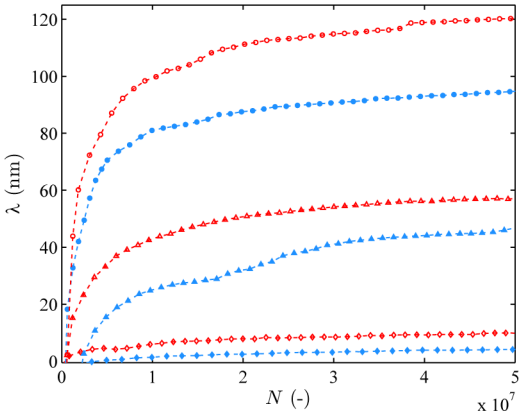

Figure 12. Delamination evolution for the examples displayed in Figure 11 for the case of $\lambda/h_{Al_2O_3}$ = 5; legend as in Figure 11.

along the microresonator's thickness are assumed to form before the occurrence of delamination, which is consistent with the results shown in Section 3.2.

(4) Delamination rates were calculated by linearly fitting the λ versus N data between λ = 0 and $\lambda = 0.7\lambda_{max}$.

The delamination rates are plotted against the strain energy release rate amplitude and displayed in Figure 13a ($\lambda/h_{Al_2O_3}$ = 5) and b ($\lambda/h_{Al_2O_3}$ = 10). The rates are roughly in the range of 1 × 10^{-8} Å/cycle to 1 × 10^{-3} Å/cycle. These very small rates mean that the delamination front does not advance uniformly along the length of the channeled crack every cycle; in other words the calculated rates represent average delamination rates along the channeled cracks. A clear environmental trend can be seen in both plots: testing in the harsh environment leads to higher delamination rates by roughly 1 order of magnitude than testing in the mild environment. Another observed trend is an increase in $d\lambda/dN$ with G_a, with roughly 3 orders of magnitude increase in $d\lambda/dN$ for an order of magnitude increase in G_a. A power fit was applied for each environment, because such relationships are typically employed to model fatigue crack

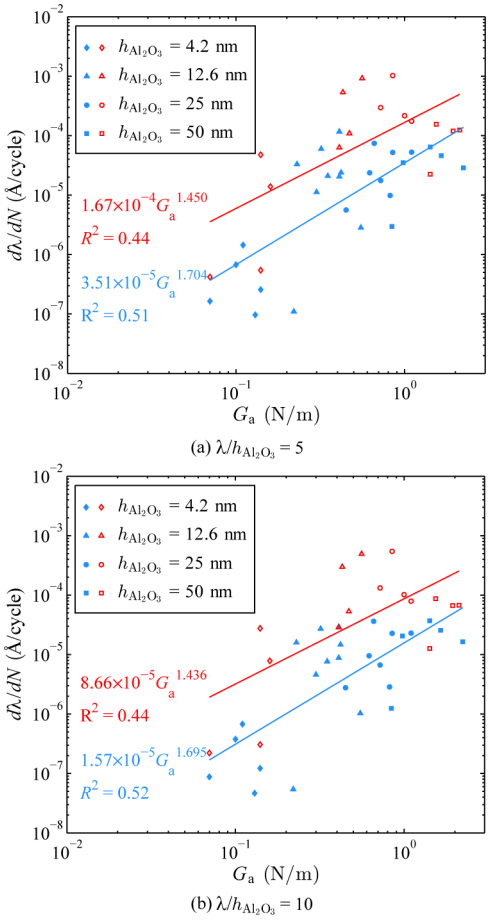

Figure 13. Average delamination rates $d\lambda/dL$ as a function of energy release rate amplitude G_a. Solid (light blue) symbols denote 30 °C, 50% RH, outlined (red) symbols denote 80 °C, 90% RH. (a) Delamination growth rates assuming $\lambda/h_{Al_2O_3}$ = 5. (b) Delamination growth rates assuming $\lambda/h_{Al_2O_3}$ = 10. The two plots' main difference is a shift to slightly higher rates (by a factor of about 2) for the model in b.

growth rates (refs 8−19). The power exponent is approximately 1.7 for the mild environment and about 1.4 for the harsh environment. It should be noted that these fits are fairly poor (R^2 = 0.52 for 30 °C, 50% RH, and 0.44 for 80 °C, 90% RH), resulting from the scatter apparent in Figure 13. It is likely that part of this scatter comes from the simplified model described above that is used to calculate the delamination rates. Particularly, the assumption of a uniform advancement of the delamination front is unlikely, as mentioned above. Regardless of this scatter, the overall trends, including the environmental effects, can still be captured with Figure 13.

4. DISCUSSION

The results presented in the previous section show that the microresonator technique is well suited for characterizing the fatigue delamination properties of ALD coatings on silicon films in a configuration relevant to MEMS devices. The four-point bending (4PB) testing technique, while very adequate to measure the interfacial fracture energies (G_c) of thin films[9] (including ultrathin films[28]), and subcritical delamination,[17] is not well suited to study fatigue properties, especially in the very high cycle fatigue regime. The magnetically actuated peel test (MAPT) is a promising technique to determine G_c as well as

both subcritical and fatigue delamination properties.[14,15] However, the MAPT technique has so far been only demonstrated for thin films on flat substrates. In contrast, the microresonator technique allows calculation of the fatigue delamination rates of ALD coatings on the rough sidewalls of DRIE silicon films, under fully reversed loading conditions, which is a configuration relevant for a large range of silicon MEMS devices. Additional advantages of this technique include the ability to perform precise and fixtureless loading (via electrostatic actuation), simple specimen fabrication (ALD coating on silicon MEMS device), relative ease of delamination propagation calculation (based on precise f_0 measurements and a validated FEM), and employability in a wide range of environments. Perhaps the main drawback of this technique is its inability to measure G_c values or subcritical delamination rates in a straightforward manner in its current version. The design of the comb drives and/or the microfabrication process would need to be modified to provide large, monotonic, electrostatically actuated loading, requiring a significant increase in the number of fingers or smaller gaps between adjacent fingers.

The microresonator technique is based on f_0 measurements (i.e., stiffness measurements) and a calibrated FEM to correlate f_0 changes with delamination length. This approach is in essence similar to the load relaxation measurement (i.e., stiffness measurements) under fixed displacement employed with the 4PB technique to calculate subcritical delamination rates. Both techniques rely on reasonable assumptions to calculate the delamination length, namely a uniform delamination front on each side of the crack. In the 4PB technique, the load relaxation (i.e., compliance change due to delamination) is significant enough that the applied driving force for delamination (G) decreases during a test until arrest of the delamination front.[9] Hence, one test can provide the full da/dt vs G subcritical crack growth curve. In contrast, the stiffness changes associated with delamination in the microresonator technique are negligible. Therefore each tested specimen represents a constant G_a fatigue test. Although the driving force remains nominally constant during a test, the delamination rates decrease with increasing delamination length (λ) as shown in Figure 12, with a significant decrease when λ reaches ~70% of λ_{max}. This result confirms that the observed delamination is unlikely to be instantaneous delamination (i.e., $G_{max} > G_c$), which is often accompanied with unstable propagation of the delamination front.[33] Instead, this result suggests that the governing mechanism for delamination is hindered as the delamination front progresses and gets farther from the channeled crack where delamination initiated.

The governing mechanism appears to be related to (cyclic) fatigue for the following reasons. First, the decrease in f_0 is gradual, requiring typically $\sim 1 \times 10^8$ cycles for the frequency to stabilize. This is consistent with the imaging of a specimen after multiple short test segments (see Figure 6), which confirmed that the damage increases with further cycling. More importantly, static loading − of both, virgin specimens (G_s = 0.53 N m^{-1}) and a specimen which had been exposed to short fatigue testing to introduce a crack (G_s = 0.63 N m^{-1}) − did not lead to a change in f_0 although fatigue loading at the same $G_a = G_s$ results in considerable changes in f_0 (>50 Hz). This result clearly indicates that time-dependent, subcritical delamination (i.e., stress corrosion cracking) cannot be the sole governing mechanism, at least for G_a below 0.5−0.6 N m^{-1}. Another result supporting this conclusion are the low values of the exponents for the da/dN vs G_a power fits (1.7 for the mild environment and 1.4 for the harsh environment), compared to typically larger values (>10) for stress corrosion cracking in ceramics.[38,39] Cyclic loading has already been demonstrated to increase the delamination rates compared to the rates measured under static loading in the case of metal/ceramic interfaces.[16] The underlying fatigue mechanism was related to the classical fatigue mechanisms of metals, which cannot be the governing mechanism for Al_2O_3 on silicon.

The observed cyclic delamination may in fact be attributed to the particular configuration of this studied interface, namely the presence of compressive loads and the roughness of the DRIE silicon film sidewall. The interface fracture energy is the sum of the intrinsic interface fracture energy (G_o) (a measure of the bonding energy at the interface), and an additional term ΔG representing processes associated with an energy dissipation zone, such as plasticity of adjacent ductile layers.[9] Here, the additional term G_c may result from interaction of the crack faces behind the delamination front, such as frictional sliding of contact asperities which would arise due to the rough silicon sidewall. It is hypothesized that this frictional sliding term ΔG degrades with further cyclic loading because of the presence of compressive loads, thereby decreasing the interface fracture resistance term G_c and leading to additional delamination. This mechanism would in essence be similar to the fatigue degradation mechanisms of extrinsically toughened ceramics due to cyclic degradation of the extrinsic toughening mechanisms.[40] Here, the cyclic compressive stresses result in repeating contact of the channeled crack's faces, which is thought to induce delamination and reduce the frictional sliding between the delaminated coating and the rough silicon sidewall. Such a process would be consistent with the elevated features observed along the delamination area (Figures 5 and 6), as well as the decreasing rates with further delamination away from the channeled crack (Figure 12).

The delamination rates were also observed to be highly dependent on the environment, with 1 order of magnitude larger rates in a harsh environment compared to the mild environment (the harsh environment consists of a modest increase in temperature (by 50 °C) and an ~20-time increase in partial pressure of water). A possible explanation for the increased rates is the occurrence of stress corrosion cracking at lower G values in the harsh environment,[17] although this should lead to large power exponents n, which is not the case. Another explanation could be related to the effect of the environment on reducing the intrinsic interface fracture resistance G_o,[9−11,17] which would lead to lower G_c values and therefore faster degradation rates for the same driving force. In any case, this result has important implications regarding the reliability of coated MEMS devices exposed to the environment.

5. CONCLUSIONS

The influence of environment (a mild (30 °C, 50% RH) and a harsh one (80 °C, 90% RH)), and coating thickness ($h_{Al_2O_3}$ = 4.2, 12.6, 25, 50 nm) on the interfacial fatigue behavior of a model ALD Al_2O_3 coating on silicon was investigated using silicon microresonators. Additionally, a few tests were conducted under static loading in laboratory air. The main findings are summarized below.

- The average delamination rates under cyclic loading are in the range of 1×10^{-8} Å/per cycle to 1×10^{-3} Å/per

cycle for 0.07 N m^{-1} < G_a < 2.23 N m^{-1}; these very low rates show that the delamination does not grow along the entire delamination front every cycle. Cyclic delamination rates are (a) environment-dependent, being roughly 1 order of magnitude higher at 80 °C, 90% RH than at 30 °C, 50% RH and (b) increase with increasing G_a, following a power law relationship with exponents of ∼1.7 for the mild and ∼1.4 for the harsh environment.

- Delamination is only observed under cyclic loading: no time-dependent delamination (nor cracking) is observed under static loading at strains of 1.51, 1.65, or −1.60%, for which cyclic loading leads to significant damage. It is believed that the combined effect of compressive load and the silicon sidewall's roughness can lead to the observed fatigue behavior.
- MEMS microresonators allow to test interfacial fatigue properties under conditions relevant to ALD-coated MEMS, such as tensile and compressive cyclic loading (stress ratio $R = -1$) at high frequencies (kHz range), accumulation of billions of cycles, rough (scalloped) silicon sidewalls, and fatigue damage accumulating on the device's sidewall. Delamination and/or cracking lead to changes in f_0, which can be both accurately measured experimentally and reliably modeled using FEM.

AUTHOR INFORMATION

Corresponding Author

*E-mail: olivier.pierron@me.gatech.edu.

Notes

The authors declare no competing financial interest.

ACKNOWLEDGMENTS

The authors thank Eric Woods and Todd Walters from Georgia Institute of Technology's Institute for Electronics and Nanotechnology for SEM imaging advice.

REFERENCES

(1) Seo, J.; Brand, O. J. *Microelectromech. Syst.* **2008**, *17*, 483−493.
(2) Hoivik, N. D.; Elam, J. W.; Linderman, R. J.; Bright, V. M.; George, S. M.; Lee, Y. C. *Sens. Actuators, A* **2003**, *103*, 100−108.
(3) Puurunen, R. L.; Saarilahti, J.; Kattelus, H. *ECS Trans.* **2007**, *11*, 3−14.
(4) Stoldt, C. R.; Bright, V. M. *J. Phys. D: Appl. Phys.* **2006**, *39*, R163−R170.
(5) Mayer, T. M.; Elam, J. W.; George, S. M.; Kotula, P. G.; Goeke, R. S. *Appl. Phys. Lett.* **2003**, *82*, 2883−2885.
(6) Budnitzki, M.; Pierron, O. N. *Appl. Phys. Lett.* **2009**, *94*, 141906.
(7) Baumert, E. K.; Theillet, P. O.; Pierron, O. N. *Scr. Mater.* **2011**, *65*, 596−599.
(8) McNaney, J. M.; Cannon, R. M.; Ritchie, R. O. *Acta Mater.* **1996**, *44*, 4713−4728.
(9) Dauskardt, R.; Lane, M.; Ma, Q.; Krishna, N. *Eng. Fract. Mech.* **1998**, *61*, 141−162.
(10) Xu, G.; He, M. Y.; Clarke, D. R. *Acta Mater.* **1999**, *47*, 4131−4141.
(11) Lane, M.; Dauskardt, R. H.; Vainchtein, A.; Gao, H. J. *J. Mater. Res.* **2000**, *15*, 2758−2769.
(12) Zhou, Y. C.; Tonomori, T.; Yoshida, A.; Liu, L.; Bignall, G.; Hashida, T. *Surf. Coat. Technol.* **2002**, *157*, 118−127.
(13) Kruzic, J. J.; McNaney, J. M.; Cannon, R. M.; Ritchie, R. O. *Mech. Mater.* **2004**, *36*, 57−72.
(14) Zheng, J. T.; Ostrowicki, G.; Sitaraman, S. K. *IEEE Trans. Compon. Packag. Technol.* **2010**, *33*, 648−654.
(15) Ostrowicki, G. T.; Sitaraman, S. K. *Thin Solid Films* **2012**, *520*, 3987−3993.
(16) Cannon, R. M.; Dalgleish, B. J.; Dauskardt, R. H.; Oh, T. S.; Ritchie, R. O. *Acta Metall. Mater.* **1991**, *39*, 2145−2156.
(17) Lane, M. W.; Snodgrass, J. M.; Dauskardt, R. H. *Microelectron. Reliab.* **2001**, *41*, 1615−1624.
(18) Hirakata, H.; Kitazawa, M.; Kitamura, T. *Acta Mater.* **2006**, *54*, 89−97.
(19) Yan, Y. B.; Sumigawa, T.; Kitamura, T. *Sci. Eng., A* **2012**, *556*, 147−154.
(20) Tripp, M. K.; Stampfer, C.; Miller, D. C.; Helbling, T.; Herrmann, C. F.; Hierold, C.; Gall, K.; George, S. M.; Bright, V. M. *Sens. Actuators, A* **2006**, *130−131*, 419−429.
(21) Jen, S. H.; Bertrand, J. A.; George, S. M. *J. Appl. Phys.* **2011**, 109.
(22) Bull, S. J. *J. Vac. Sci. Technol., A* **2012**, *30*, No. 01A160.
(23) Miller, D. C.; Foster, R. R.; Zhang, Y. D.; Jen, S. H.; Bertrand, J. A.; Lu, Z. X.; Seghete, D.; O'Patchen, J. L.; Yang, R. G.; Lee, Y. C.; George, S. M.; Dunn, M. L. *J. Appl. Phys.* **2009**, *105*, 12.
(24) Tapily, K.; Jakes, J. E.; Stone, D. S.; Shrestha, P.; Gu, D.; Baumgart, H.; Elmustafa, A. A. *J. Electrochem. Soc.* **2008**, *155*, H545−H551.
(25) Miller, D. C.; Foster, R. R.; Jen, S. H.; Bertrand, J. A.; Cunningham, S. J.; Morris, A. S.; Lee, Y. C.; George, S. M.; Dunn, M. L. *Sens. Actuators, A* **2010**, *164*, 58−67.
(26) Ou, K.; Lin, I.; Wu, P.; Huang, Z.; Chen, K.; Zhang, X. *Mater. Res. Soc. Symp. Proc.* **2009**, *1222*, 111−116.
(27) Baumert, E. K.; Pierron, O. N. *Appl. Phys. Lett.* **2012**, *101*, 251901.
(28) Birringer, R. P.; Chidester, P. J.; Dauskardt, R. H. *Eng. Fract. Mech.* **2011**, *78*, 2390−2398.
(29) Theillet, P. O.; Pierron, O. N. *Appl. Phys. Lett.* **2009**, *94*, 181915.
(30) Straub, T.; Theillet, P. O.; Eberl, C.; Pierron, O. N. *J. Microelectromech. Syst.* **2013**, *22*, 418.
(31) Burns, D. J.; Helbig, H. F. *J. Microelectromech. Syst.* **1999**, *8*, 473−482.
(32) Baumert, E. K.; Theillet, P. O.; Pierron, O. N. *Acta Mater.* **2010**, *58*, 2854−2863.
(33) Freund, L. B.; Suresh, S. *Thin Film Materials: Stress, Defect Formation, And Surface Evolution*; Cambridge University Press: Cambridge, U.K., 2003.
(34) Hull, R. I. I. S. *Properties of Crystalline Silicon*; EMIS datareviews series; The Institution of Engineering and Technology: Herts, U.K., 1999; Vol. *20*.
(35) Suo, Z. G.; Hutchinson, J. W. *Int. J. Fract.* **1990**, *43*, 1−18.
(36) Hosseinian, E.; Theillet, P. O.; Pierron, O. N. *Sens. Actuators, A* **2013**, *189*, 380−389.
(37) Evans, A.; Fuller, E. *Metall. Trans.* **1974**, *5*, 27.
(38) Bhatnagar, A.; Hoffman, M. J.; Dauskardt, R. H. *J. Am. Ceram. Soc.* **2000**, *83*, 585−596.
(39) Wiederhorn, S. M. *J. Am. Ceram. Soc.* **1967**, *50*, 407−414.
(40) Ritchie, R. *Int. J. Fract.* **1999**, *100*, 55−83.